Cool running: Passive radiative cooling to sub-ambient temperatures inside naturally ventilated buildings

Remy Fortin[a], Jyotirmoy Mandal[b], Aaswath P. Raman[c], Salmaan Craig[d,1]

[a] School of Architecture, McGill University, Montréal, QC, Canada

[b] Department of Civil & Environmental Engineering, Princeton University, Princeton, NJ, USA

[c] Department of Materials Science and Engineering, University of California, Los Angeles, Los Angeles, CA, USA

[d] Department of Civil Engineering, McGill University, Montréal, QC, Canada

[1] Corresponding author: salmaan.craig@mcgill.ca

Abstract. One priority for avoiding runaway climate change is finding viable alternatives to mechanical air-conditioning. Recent advances in daytime radiative cooling materials are promising. However, researchers have not yet shown how to use them for passive cooling below ambient temperature *indoors*. Ventilation is challenging in this regard as healthy air changes will heat the sub-ambient interior. We present a field study using analog models to observe how daytime radiative cooling materials can passively reject heat from inside naturally ventilated buildings. We mounted two test boxes on a rooftop in Southern California, replicating in miniature the thermal loads, losses, and air changes for one occupant. The control box represented a reference 'gold standard' for passive cooling: internal thermal mass with night ventilation. The test box had an uninsulated metal roof with a top surface for daytime radiative cooling. Both boxes had internal heat sources with ventilation driven not by wind but by buoyancy. Under clear skies, the test box maintained an interior temperature of 3.9 +/- 4.8 °C *below* the mean prevailing exterior temperature while venting 6.9 +/- 0.3 air changes per hour during the day. In comparison, the control box maintained an interior temperature of 5.0 +/- 1.7 °C *above* the mean prevailing exterior temperature while venting 8.6 +/- 0.1 air changes per hour during the night. We show with a calibrated model how to improve the sub-ambient temperature stability of the test box with more thermal mass in the roof and how to scale up the results to actual buildings.

Significance Statement. In a warming world, new passive cooling techniques could help curtail the growing demand for mechanical air-conditioning and the resulting emissions that further heat the planet. Recent breakthroughs in passive radiative cooling materials, which reflect sunshine while emitting infrared heat into cold outer space, show promise. But it's unclear how these materials could replace mechanical heat rejection in well-ventilated buildings. In a field experiment with two model buildings, each scaled to one person's heat load and fresh air needs, we show how to chill the air below the ambient temperature inside a naturally ventilated enclosure by coupling terrestrial radiation, thermal mass, and gravity-driven air changes, while outperforming a reference 'gold standard' for passive cooling.

Keywords: Radiative cooling. Natural ventilation. Thermal comfort. Energy efficiency.

Introduction

Climate change is driving demand for mechanical air-conditioning while the growing greenhouse gas emissions from using and making these systems, not least from leaking refrigerants (1), further heat the planet (2, 3). Several breakthroughs in passive radiative cooling materials, which reflect sunshine like a mirror while emitting infrared heat into cold outer space through the atmospheric window, have been made recently (4–11). However, if these materials can augment or replace mechanical heat rejection in buildings (12–16), it is unclear how and where or for which occupancy types, especially now that healthy ventilation with plentiful air changes is a priority (17).

With some success, daytime radiative cooling materials and coatings have been added to the outside of insulated roofs (14–16, 18), improving the energy efficiency of entire building stocks. However, true cooling entails removing heat, which is more challenging than improving protection from overheating. On a hot day, these surface treatments can only reduce the temperature difference across the exterior insulation, rejecting little to no heat from the interior. Some researchers, including Felix Trombe, often cited as the first pioneer of radiative cooling, have explored removing insulation from sky-facing surfaces to reject heat from the interior (Figure 1A to C) (15, 19–22). While these test enclosures produced sub-ambient temperatures, the need for ventilation, and its effect on the heat balance, seems to be a crucial oversight in the experiments.

Not all buildings are mechanically ventilated and air-conditioned, particularly in developing countries. The current 'gold standard' for passive cooling in hot and dry climates (assuming water is too precious to evaporate as a spray (23)) is an internal thermal mass with night ventilation (24–27). The thermal mass, protected by external insulation, absorbs internal heat from people, devices, lighting, and so on, while the ventilation lets the mass discharge this heat at night. Even simpler, the ventilation may be driven naturally by a combination of wind and buoyancy forces (28–30). In this study, we examine how to surpass this 'gold standard' for passive cooling by adding 24-hour radiative cooling from an uninsulated roof. We experimentally demonstrate a model enclosure that maintained an interior temperature of 3.9°C below the mean prevailing exterior temperature while consistently venting nearly 7 air changes per hour during the day. Our results demonstrate that it is in fact possible to passively maintain structures in the built environment cooler than their ambient using passive radiative cooling while also ensuring adequate ventilation from the exterior.

Heat balance

For this purpose, we define the evolution of the air temperature inside a ventilated enclosure as

$$\rho Cp_{in}\, V_{in}\, \frac{dT_{in}}{dt} = W_V + W_M + W_R + W_E + W_H \qquad (1)$$

where ρCp_{in} is the volumetric heat capacity of the air, V_{in} is the volume of interior air, W_V, W_M and W_R are the internal heat exchanges with the ventilation, thermal mass, and the underside of the roof, respectively, W_E is the heat transfer through the insulated external walls, and W_H is the internal heat generated by people, devices, and so on.

Not only do we wish to put the interior space in radiant communication with outer space via the roof, but we also want to put the interior air in fluid communication with the atmosphere. In the heat balance of Eq. 1, ventilation (W_V) heats or cools the interior depending on its sign (i.e., the relative temperature of the exterior). Ventilation is necessary for health reasons, as the COVID-19 pandemic has highlighted. We wish to understand how to achieve passive cooling to sub-ambient indoor temperatures without sacrificing healthy air changes. The geographical limits and practical applications may be evaluated once this physical balance is understood.

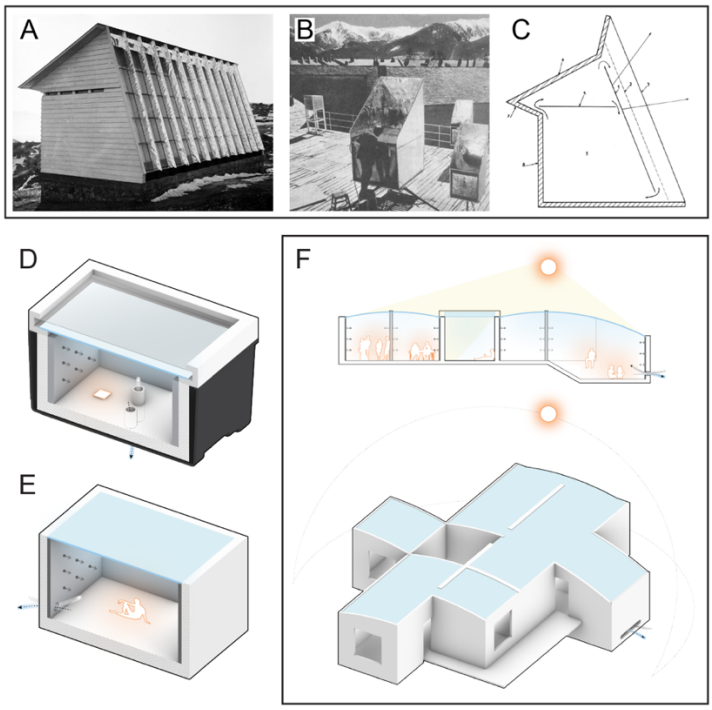

Figure 1. Passive radiative cooling in unventilated and ventilated enclosures. **(A)** North-East view showing the radiative cooling façade of the cold house designed and built by Felix Trombe and his team in 1963-63 in Odeillo, France (21). **(B)** View of an experimental cooling container used by Trombe and his team in Mont-Louis, France, undated (22). **(C)** Diagrammatic vertical section of Trombe's patented design for the cold house, 1967 (19). **(D)** Schematic drawing of our experimental box showing how the water bottles can be replaced by an equivalent concrete thermal mass. **(E)** Schema of the proportions required for the thermal mass, radiator, and ventilation openings to match the thermal loads, losses, and air changes attributable to one occupant **(F)** Schematic section and axonometric view of an architectural concept for a 10-people building.

The driving force for buoyancy ventilation can be formulated as a 'reduced gravity,' $g' = g\beta\Delta T$, where g is the gravitational acceleration, β is the coefficient of thermal expansion of air, and $\Delta T = T_a - T_{in}$ is the difference between ambient and indoor air temperature. The heat exchanges from the ventilation W_V is then calculated from the natural ventilation flow rate Q as

$$Q = A^* \sqrt{\left|\frac{\Delta pw - g'H}{\rho}\right|} \qquad (2)$$

$$W_V = \rho C p_{in} \Delta T \, Q \qquad (3)$$

where A* is the effective size of the ventilation openings, Δpw is the wind pressure difference between the openings, *H* is the height between the openings, and ρ is the air density. Wind and buoyancy forces may complement or compete with each other, depending on the vent locations and their orientation to the wind. Later, we design the vents to eliminate the influence of wind. In any case, we model the internal thermal mass as lumped, that is, neglecting the diffusion of heat through the mass, to simplify the thermal coupling with buoyancy ventilation

$$\rho Cp_M V_M \frac{dT_M}{dt} = -W_M \quad (4)$$

$$W_M = S_M h_M (T_M - T_{in}) \quad (5)$$

where T_M is the mass temperature, ρCp_M is the heat capacity of the thermal mass, V_M is the thermal mass volume, S_M is the surface area in contact with the indoor air, and h_M the heat transfer coefficient to and from the surface of the thermal mass which is in contact with the interior air. We also model the thermal mass in the roof-radiator as a lumped mass

$$\rho Cp_R V_R \frac{dT_R}{dt} = W_{sky} - W_R \quad (6)$$

$$W_R = S_R h_R (T_R - T_{in}) \quad (7)$$

where the subscript R indicates the equivalent parameters for the radiator as for the thermal mass in Eq. 4 and 5, and W_{sky} is the balance of thermal radiation, solar radiation, and convection on the top surface of the radiator, defined below. We now report our experiment, investigating the coupling of thermal mass, buoyancy ventilation, and radiative cooling in passive building design. We show how to maintain sub-ambient interior temperatures while producing steady air changes, with results that scale to per-person heat loads and fresh air requirements.

Results

We installed two insulated boxes in a warm, dry climate (Topanga Valley, CA) with an open view of the sky (Figure 2). The first box, hereafter called the control box, had an internal thermal mass, an internal heat source, and two upward-pointing ventilation stacks. In this box, ventilation only occurred when the buoyancy pressure was negative, that is, when the interior temperature was warmer than the exterior, prompting upward flow through the shortest pipe-vent (Figure 2A and C). The other box, hereafter called the test box, had the same thermal mass and internal heat source, but the roof was an uninsulated aluminum plate with a daytime radiative cooling material glued to its top surface (Materials and Methods). The underside (soffit) of the radiator was directly coupled to the interior by natural convection. Its sky-facing side had an infrared-transparent guard above it to limit convective heating from the exterior.

In the test box, the ventilation stacks pointed downward so as not to interfere with the radiator. As a result, the ventilation was only triggered when the interior temperature was cooler than the exterior. As such, the ventilation of both boxes was driven by the temperature difference between inside and outside, but for opposite signs, biasing the control box for night venting and the test box for day venting. In this way, both boxes could reach their lowest temperatures while still providing a healthy rate of ventilation for half a daily cycle.

We scaled the experiment targeting a flow rate of ~0.1 l/s (liters/second), representing 1% of the ventilation rate that is required by one person. (Engineering guidelines recommend 10 l/s per person in non-residential buildings, although these rates are likely to increase to 14 l/s following the COVID-19 pandemic (17).) Meanwhile, the differential height of the pipe-vents helped to drive the buoyancy flow, promote good mixing of the interior air by the incoming plume, and ensure unidirectional flow through each pipe-vent for measurement purposes (30). The closeness of the pipes to each other, and the fact they hardly protruded outside the box (as shown in Figure 2A to D) helped to eliminate differential wind pressure (25, 31).

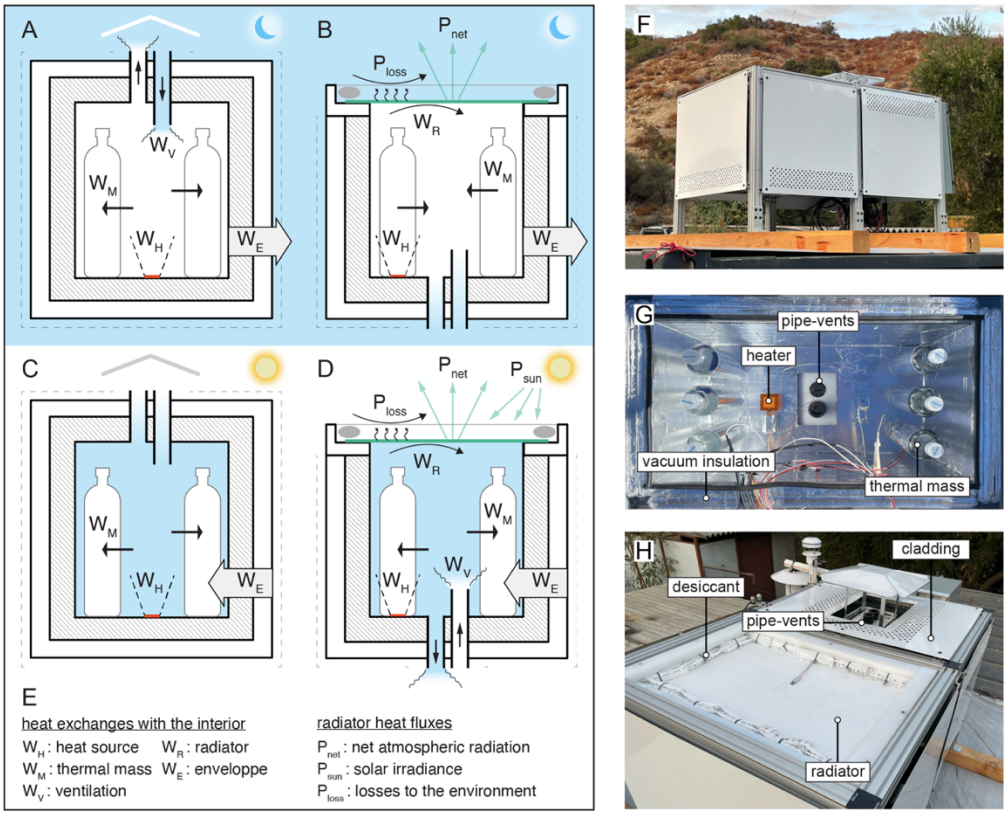

Figure 2. **(A)** Control box at night. Upward mixing ventilation when the interior is warmer than the exterior. **(B)** Test box at night. No ventilation when the interior is warmer than the exterior. **(C)** Control box during day. No ventilation when the interior is cooler than the exterior. **(D)** Test box during day. Downward mixing ventilation when the interior is cooler than the exterior. **(E)** Nomenclature **(F)** Photo of the experiment setup in Southern California. **(G)** Annotated photo of the interior of the test box. **(G)** Annotated photo showing the radiator on top of the test box (front) and the high-level pipe-vents of the control box (back).

The thermal mass inside each test box was a set of water bottles, chosen for cost, simplicity, and volumetric heat capacity. The thermal mass, ventilation flow rate, and roof radiator were sized so that all the heat exchanges with the interior (listed in Eq. 1) were reduced by the same order of magnitude, representing approximately one percent of the heat load and ventilation requirements typically associated with one occupant. Since ventilation exchanges were potentially the most challenging to get right, we started with Eq. 2, sizing the cross-sectional area and length of the pipe-vents to achieve a flow rate of ∽0.1 liter/sec (the equivalent of 10 liter/sec. at building scale), assuming no wind and a 5 °C temperature difference with the exterior. Then, we calculated the radiative cooling roof area (S_R) needed to offset an internal heat source of 1.2 W (or 120 W) based on simulations for W_{sky} and the properties of the daytime radiative cooling material (described in Materials and Methods). In parallel, we used thermal mass scaling rules as a starting point to determine the surface area (S_M) and volume (V_M) of internal mass that would be needed to keep the interior temperature within a ∽5 °C range under an exterior temperature swing of ∽15 °C (26). Finally, we input those values into our theoretical model (Eq. 1 to 7) and proceeded by iteration to find the combination that would be both practical and produce the coldest and most stable interior temperature.

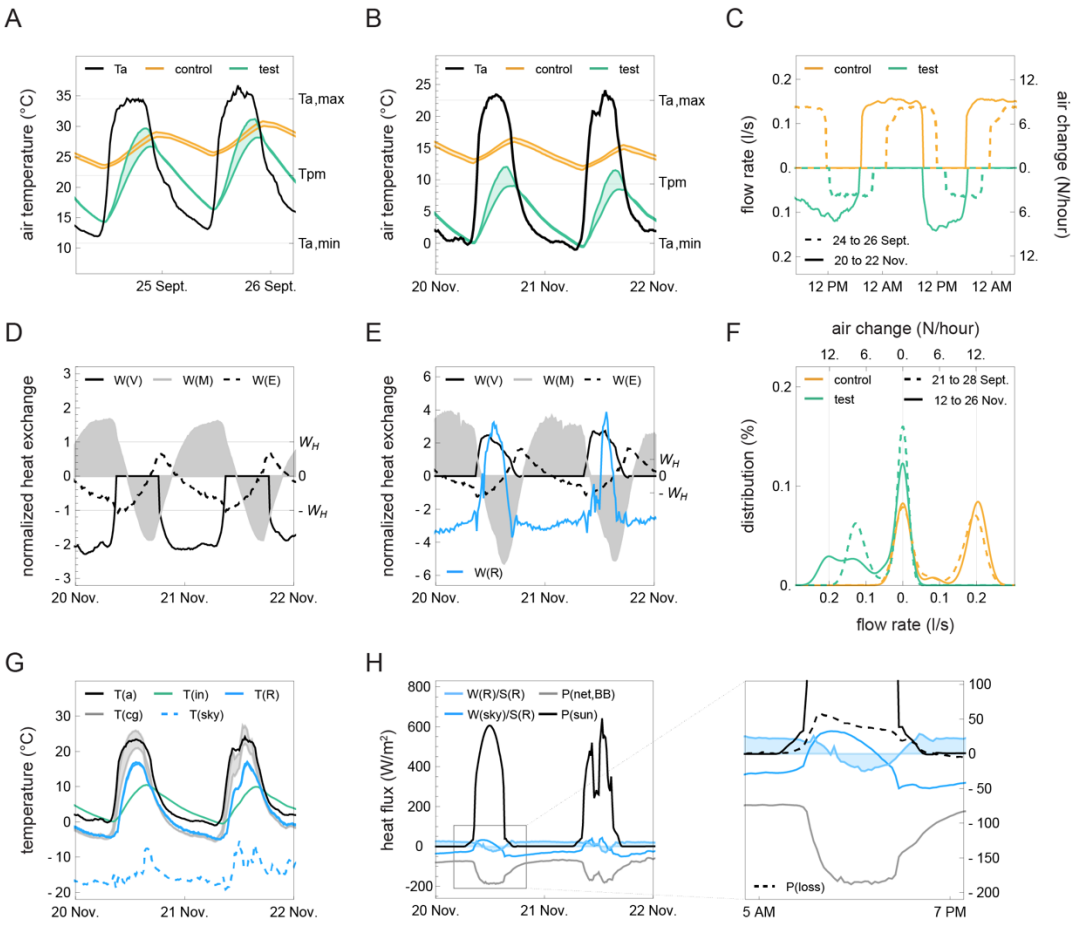

Figure 3. Temperature, ventilation flow and heat exchange measurements. **(A)** Air temperature T_{in} inside the control and test boxes with ambient temperature T_a for two typical days in September 2022, when the mean prevailing ambient temperature T_{pm} was 21.9 °C, with an average of 23.7 °C between the daily maximum and minimum T_a. **(B)** Typical variations of T_{in} and T_a for two days in November 2022, after 1.5 times more thermal mass added in both boxes. T_{pm} was 9.4 °C, and the difference between the daily maximum and minimum T_a was 22.4 °C. The interior of the control and test boxes varied on average 5.0 +/- 1.7 °C above and 3.9 +/- 4.8 °C. **(C)** Comparison of the ventilation flow rate Q and the number of air changes per hour in the control and test boxes for two typical days in September and November 2022. Since T_{in} is more stable in November, the temperature difference between T_a and T_{in} increases, and so does the ventilation rate. **(D)** Normalized heat exchanges inside the control box during two typical days in November 2022 (scaled to W_H = 1.2 W). **(E)** Normalized heat exchanges inside the test box during two days in November 2022 (scaled to W_H = 1.2 W). Note the change in x-axis scale **(F)** Comparison of the distribution of the ventilation flow rate Q and the number of air changes per hour during the 7-day and 14-day experiments in September and November 2022. **(G)** Radiator temperature T_R with the ambient air temperature T_a, indoor air temperature T_{in}, air temperature inside the convection guard T_{cg}, and effective sky temperature T_{sky} for two typical days in November 2022. **(H)** Measured heat fluxes on the top surface (W_{sky}/S_R) and soffit (W_R/S_R) of the radiator, with downward solar radiation flux *Psun*, net atmospheric radiation flux for a blackbody at ambient temperature $P_{net,BB}$, and predicted parasitic losses through the convection guard P_{loss} for two typical days in November 2022 and from 5 AM to 7 PM on November 20.

Temperature and flow rate

We ran two experiments under clear sky conditions and measured the air temperature and ventilation exchanges inside the boxes, as well as the other heat exchanges expressed in Eq. 1. During the first experiment in September, the interior temperature of the control box fluctuated 4.3 +/- 2.5 °C above the mean prevailing ambient temperature T_{pm} (Figure 3A). (Note that the error reported here represents the difference between the mean daily maximum and minimum temperatures). In comparison, the test box remained 1.6 +/- 6.8 °C below T_{pm} (Figure 3A). The

interior temperature of the test box was less stable than the control box, and its peak temperature occasionally exceeded that of the control, so we decided to add 1.5 times more thermal mass in the boxes to further stabilize their interior temperature in a second experiment. This took place in November, and the interior of the control box fluctuated 5.0 +/- 1.7 °C above T_{pm} while the extra mass helped dampen the interior temperature swing ($T_{in,max} - T_{in,min}$) by factor 0.86 relative to the exterior. The test box varied on average 3.9 +/- 4.8 °C below T_{pm} and reduced the ambient temperature swing ($T_{a,max} - T_{a,min}$) by a factor of 0.59 (Figure 3B). The relative instability of the test box was caused by the variation in the radiator temperature since the test box had the same amount of internal thermal mass as the control box.

The ventilation stacks in both boxes were designed to produce unidirectional, wind-insensitive ventilation and well-mixed thermal conditions inside the boxes (Materials and Methods). As intended, the ventilation did occur over half-day cycles based on the temperature difference between the inside and outside (Figure 3C and 3F). In September, the control box vented on average 0.133 +/- 0.015 l/s during the day, and the test box vented 0.061 +/- 0.013 l/s during the night. (Note that the error reported here represents the reading error from the sensors, which was greater than the standard deviation.) In comparison, the control box vented 0.143 +/- 0.015 l/s during the day, and the test box vented 0.115 +/- 0.014 l/s during the night in November. Since the air temperature was more stable inside the control box, it led to a bigger temperature difference with the outside and larger ventilation flow rates. Similarly, the temperature variations in the control and test boxes were dampened by the additional thermal mass in November and therefore produced more ventilation.

Interior heat balance

Along with the temperature and ventilation flow measurements, we measured all the components of the heat balance in Eq. 1 (Materials and Methods). In the control box, the internal thermal mass produced alternating heating and cooling cycles (W_M), depending on whether it was warmer or cooler than the interior (Figure 3D). Because the ventilation only occurred when the inside of the box was warmer than the ambient air, the thermal mass cooled down at night faster than it warmed up during the day, biasing the system towards cooler temperatures.

In the test box, the heat absorbed by the thermal mass from ventilation changes during the day was discharged by the radiator at night, through a combination of convection and radiation, or just radiation, depending on the temperature of the radiator. However, the roof thermal mass did overheat (W_R > 0) in the afternoon when the solar loads were particularly strong, and when the interior temperature was at its coolest relative to the ambient (Figure 3E). At these times, the internal thermal mass (W_M) absorbed most of the heat brought in by ventilation, and the thermal inertia of the indoor air cooled the roof (W_R), not the other way around.

Radiator fluxes

While the interior cooling power of the radiator was on average 1.9 times more than the heating power from the heat source, this cooling was somewhat inconsistent (Figure 3E). As a result, the internal thermal mass would cool down at night faster in the test box than in the control box, but it also warmed up faster during the day, so its stabilizing effect was limited. In this regard, it is important to understand how to potentially stabilize the roof temperature, which is not obvious with conjugate heat exchanges occurring simultaneously on both sides (Eq. 6). The balance of the radiation and convection fluxes at the top surface of the radiator (W_{sky}) may be calculated from the effective sky temperature T_{sky} as

$$T_{sky} = ({T_a}^4 - P_{net,BB}\sigma^{-1})^{1/4} \quad (8)$$

$$W_{sky} = S_R\,(\epsilon\,\sigma\,({T_R}^4 - {T_{sky}}^4) - \alpha\,P_{sun} - P_{loss}) \quad (9)$$

where ϵ is the hemispherical emissivity of the roof surface (Materials and Methods), $P_{net,BB}$ is the net atmospheric radiation flux for a blackbody at ambient temperature, $\alpha\,P_{sun}$ is the absorbed solar radiation flux based on the surface's solar absorptivity α (Materials and Methods), and P_{loss} is the sum of parasitic losses to the environment, including convection and re-radiation from the convection guard.

In the November experiment, the radiator temperature (T_R) followed the ambient temperature (T_a), but remained on average 6.4 °C and 3.7 °C cooler under peak solar irradiance and during the night, respectively (Figure 3G). Even though T_R stayed below the ambient temperature throughout the experiment, it followed the ambient temperature closely, causing it to overshoot the indoor air by up to 9.5 °C in the afternoon. This instability was not helped by overheating inside the convection guard ($T_{cg} > T_a$), which exceeded the ambient temperature by up to 4°C in the afternoon, adding unnecessary heat to the radiator (see P_{loss} in Figure 3H).

Interior temperature stability

To further analyze the sub-ambient temperatures inside the experiment boxes, and understand if they could have evolved with more stability, it is useful to normalize the interior temperature as

$$\theta = (T - T0)/\Delta T_a \quad (10)$$

where $T0 = (T_{a,max} + T_{a,min})/2$, is the daily mean ambient temperature and $\Delta T_a = |T_{a,max} - T0|$ is the daily ambient temperature increment above the mean. In Figure 4, we compare these temperatures with the prevailing mean ambient temperature, which serves as a reference in the ASHRAE adaptive comfort standard for naturally ventilated buildings (32). This design standard reflects empirical evidence that peoples' thermal expectations change with the predominant weather and allows a 5-7°C range of acceptable indoor temperatures (33, 34). The upper and lower limits to keep at least 80% of the occupants comfortable are

$$T_{op,min} = 14.3 + 0.31\,T_{pm} \quad (11)$$

$$T_{op,max} = 21.3 + 0.31\,T_{pm} \quad (12)$$

where T_{op}, is the indoor operative temperature (a composite of the radiant and air temperature), and T_{pm} is the prevailing mean ambient temperature (defined as the average of the daily mean outdoor temperature for a sequence of 7 to 30 days (32)). It's worth noting that in the range 20.7 °C < T_{pm} < 30.9 °C, an interior temperature equal to the prevailing mean is comfortable. Above this threshold (T_{pm} > 30.9 °C), the interior space needs to be cooled below the prevailing mean, working against daytime ventilation (W_V), which will act as a heat gain.

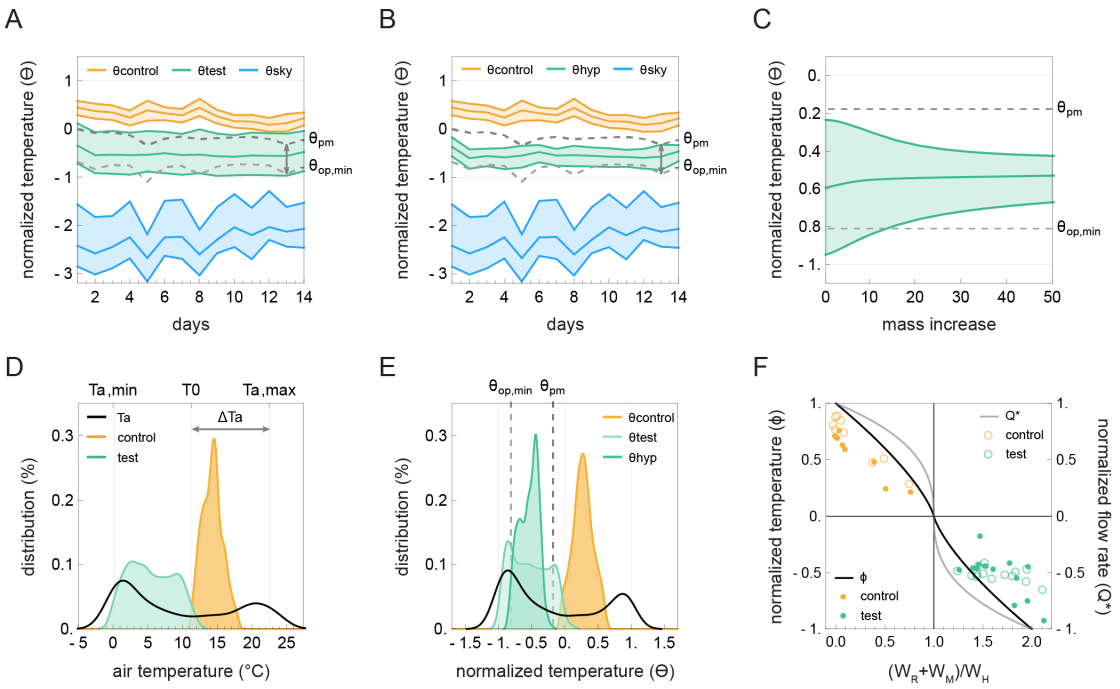

Figure 4. Interior temperature stability and prediction for a massive roof radiator. **(A)** Daily mean, max and mean temperatures inside the control (yellow) and test box (green), with the effective sky temperature (T_{sky}, Eq. 8) from November 12 to 26 2022. All temperatures are normalized based on relative to the ambient temperature using Eq. 10. The width of each band indicates the daily max. and min. temperature. The two dashed gray lines are the prevailing mean ambient temperature Θ_{pm}, and the normalized lower limit for adaptive comfort $\Theta_{op,min}$ when T_{pm} = 30.9 °C and $\Theta_{pm} = \Theta_{op,max}$. **(B)** Predictions from our calibrated model showing the interior temperature of the test box (green) with a twenty-fold increase in the roof's thermal mass. **(C)** Influence of the roof's mass increase on the mean, max. and min. temperatures inside the test box. **(D)** Distribution of T_{in} and T_a from November 12 to 26, 2022. **(E)** Distribution of the normalized temperature inside the control (yellow) and test (light green) boxes with ambient temperature Θ_a and the hypothetical scenario with more thermal mass in the roof (green). **(F)** Influence of the relative cooling $(W_R + W_M)/W_H$ on the daily mean temperature and ventilation flow rate inside the control (yellow) and test (green) boxes. Normalizations defined in text.

As Figure 4A shows, the mean temperature in the test box stayed below the prevailing mean (θ_{pm}) for the 14 days during the November experiment, while the control box stayed above this threshold. (Note that, while T_{pm} is a constant, θ_{pm} varies slightly day to day in Figure 4A and B because it is normalized for daily values of $T0$ and ΔT_a.) For reference, the scale 0 to 1 represents a temperature difference of 11.4 +/- 1 °C, where the reported error is the standard deviation between daily values of ΔT_a.

With these normalized temperatures, we can see what the performance might be like in a similar climate during a hot period (T_{pm} > 30.9 °C), relative to the prevailing mean and the current 'gold-standard' (thermal mass and night ventilation). While the consistent sub-ambient temperatures are promising, their variability day and night could cause discomfort (Figure 4A).

One way to improve the indoor temperature stability is to add more thermal mass to the roof, which we explored theoretically after calibrating our model (Eq. 1 to 7) to the experimental data. We achieved this calibration by finding the heat transfer rates on the surface of the internal thermal mass that minimized the error between W_M measured and predicted from Eq. 5 (Figure 5E). We defined that error as the root mean square error

$$RSME = \sqrt{\frac{\sum_{t=1}^{T}(P_{meas,t} - P_{pred,t})^2}{T}}$$

(13)

where T is the duration of the experiment, and $P_{meas,t}$ and $P_{pred,t}$ are the measurements and predictions at time t during the experiment. We repeated the same process for W_R on the radiator soffit, but with two convection rates, one for the period during the day when $T_R > T_a$, and one for the night when $T_a > T_R$, to account for the different modes of surface convection (Figure 5F). For W_{sky} on the sky-facing surface of the radiator, we found the effective heat transfer rate for $P_{loss} = h\,(T_a - T_R)$ that would minimize the error between W_{sky} measured and predicted from Eq. 9 with on-site measurements of P_{sun} and $P_{net,BB}$ (Figure 5F). In this case, calibrating P_{loss} for two heat transfer coefficients, to capture two convection regimes day and night, did not improve the fit between the predictions and the measurements, since T_R remained sub-ambient throughout the experiment. Furthermore, for simplicity, we assumed P_{loss} to be a function of T_a (instead of T_{cg}).

In Figure 4B, we used our calibrated model to predict the temperature inside the test box assuming the roof radiator was twenty times thicker and therefore had twenty times more thermal mass ($\rho C p_R V_R$). In this scenario, the aluminum sheet would increase from 6 to 120 mm. This extra mass stabilizes the roof temperature around a daily mean which, in turn, stabilizes the convective heat exchanges with the interior (W_R). For reference, a concrete roof that was 129 (+/- 22) mm thick, where the uncertainty depends on the thermal properties, would have the same volumetric heat capacity per unit area (35). As shown in Figure 4C, the amount of thermal mass in the roof can be tuned for different objectives. The mean interior temperature does not significantly vary after a six-fold mass increase, and there are diminishing returns with interior temperature stability after a twenty-fold mass increase. These results help evaluate the cooling potential of additional roof thermal mass alongside broader architectural considerations, such as the roof's structural performance and its embodied carbon footprint.

In Figure 4E, we compare the distribution of the normalized temperature for the test radiator (light green) and the hypothetical radiator with more mass (green). The latter is stable enough to remain within the range of adaptive comfort while also staying below the prevailing mean ambient temperature. As such, Figure 4E suggests that stable, sub-ambient cooling is possible below the prevailing mean. In dry climates, this can be useful for maintaining comfort in hot periods (T_{pm} < 32°C) according to international standards for adaptive thermal comfort in naturally ventilated buildings (32). Note that the prevailing mean (T_{pm}) is not the same as the peak exterior temperature on any given day. Therefore, this approach could still work as peak exterior temperatures approach 37°C, so long as the night temperatures are sufficiently cool. In cases where the prevailing mean or peak exterior temperatures are too high to stay within the adaptive comfort threshold, this approach could still produce interior temperatures that are cooler and, therefore, safer during dangerous heat waves. In these extreme cases, ventilation rates could be reduced to maintain cooler temperatures.

Seasonal adaptation

Finally, in Figure 4F we consider the influence of the relative cooling $(W_R + W_M)/W_H$ on the daily mean temperature and ventilation flow rate inside both boxes, following the scaling by Chenvidyakarn & Woods (28, 36, 37). The temperatures are normalized with $\phi = (T_{in} - T_a)/\Delta T_0$ and the flow rates are normalized with $Q^* = Q/Q_0$ where ΔT_0 and Q_0 are the reference temperature difference and flow rate. The reference state is an idealized steady-state condition, neglecting heat exchanges from the envelope and thermal mass and assuming the cooling W_C and heating W_H are independent variables and the ventilation is powered by the resulting temperature excess, such that $\phi = \left(1 - \frac{W_C}{W_H}\right)^{1/3}$ and $Q^* = \left(1 - \frac{W_C}{W_H}\right)^{2/3}$. In the upper limit, when there is no cooling $W_C = 0$, $\phi =$

1 and $Q^* = 1$. The measurements shown in Figure 4F are daily averages. The upper left quadrant on the phase diagram represents scenarios where heating dominates, and the buoyancy forces promote upward flow. The lower right quadrant represents scenarios where cooling dominates, and the buoyancy forces promote downward flow. This scaling is useful for two things. First, for initial design, before detailed simulation, to estimate the size of the radiator in relation to the internal heat loads, thermal mass, and ventilation rate. Second, for considering measures to switch between passive heating and cooling modes with the change of seasons, such as adjusting the vents to vary the ventilation rate, letting low-angle winter sunshine enter the building, or speculating on new technologies for adaptive insulation and switchable spectral properties.

Discussion

Our experiment suggests it is possible to cool a naturally ventilated building below the prevailing ambient temperature, using an uninsulated roof to passively reject heat to the sky and through the atmospheric window, day and night. We showed how to do this while maintaining steady air changes, using natural mixing ventilation, and how to harness these buoyancy forces in upward or downward flow, independent of wind effects. We compared the results with a control box representing the current 'gold standard' for passive cooling, which is an internal thermal mass with night ventilation. The test box was markedly cooler than the control box, but the interior temperature was less stable. Therefore, we used a calibrated model to show how adding thermal mass to the roof-radiator could stabilize the temperature evolution of the interior air, resulting in a temperature range that is narrow like the 'gold standard', but still well below the prevailing mean.

	1:100	1 pers.	10 people
Ventilation flow rate, *Q* (l/s)	0.1	10	100
Buoyancy height, *H* (m)	0.134	0.3	0.3
Effective vent area, *A** (m^2)	0.001	0.035	0.35
Thermal mass thickness, l_M (m)	0.03	0.03	0.03
Thermal mass surface, S_M (m^2)	0.396	39.6	396
Radiator surface, S_R (m^2)	0.155	15.5	155

Table 1. Scaling up the dimensions of the test box.

The design of our experiment makes it possible to scale the results to consider the dimensional implications for real buildings. To meet the cooling needs of one person, based on our test box, the surface area of internal thermal mass would be approximately 40m^2 per person, assuming a similar heat storage capacity per unit area as in the experiment, while the radiator surface would be approximately 16m^2 per person (Figure 1E and Table 1). These calculations assume a ventilation rate ($W_V / \rho C p_{in} \Delta T$) of 10 liters per second per person, and an internal heat generation rate (W_H) of 120 Watts per person.

We also simplified our simulations by using constant, albeit calibrated, heat transfer coefficients, knowing that, in reality, they depend on how the temperature difference evolves (e.g. $h \propto \Delta T^{1/4}$ for natural convection) and that we had used infrared reflective tape to eliminate radiant heat transfer inside the box. It is important to bear these nuances in mind when scaling up, as the model is sensitive to the heat transfer coefficients (as indicated in Figures 5E and 5F). For example, with natural convection on horizontal surfaces, both flow states, a quiescent boundary layer or entrainment from disorderly plumes, are self-similar with growing plate size (38). However, on vertical surfaces, the height influences the transition to turbulence and, in a naturally ventilated enclosure, the entrainment from a 'peeling onion' boundary layer (39).

One can consider substituting many kinds of thermal mass materials while scaling up. For example, the water bottles used as internal thermal mass could have been replaced by ~3cm thick concrete panels in the experiment, and we have assumed this thickness of concrete in our hypothetical scenarios for multiple occupants in Figure 1F. However, it is important to note that our model assumes a lumped thermal mass with a notional thickness expressing the ratio between the mass's volume and surface area in contact with the indoor air ($l_M = V_M/S_M$). This assumption is valid for sufficiently low Biot numbers, when the temperature gradients inside the mass are negligible. But for thicker construction elements, such as concrete floor slabs, it is necessary to account for heat diffusion, which results in lower efficacy because isotherms take several hours to travel through the mass (24). Likewise, the effective size of the ventilation openings A^* does not scale proportionally with the flow rate, but rather depends on the height of the buoyancy column driving the ventilation and the pressure losses through the ventilation loop (Materials and Methods).

The value of infrared transparent convection guards in radiative cooling assemblies has been a sticking point in the literature thus far (40). In theory, they should make the radiator more effective when it operates below ambient temperature, guarding against wind and promoting quiescence in the air gap for some insulating effect. However, when the radiator is above ambient temperature, convection helps cool it, while any re-radiation from the guard will diminish the radiator's ability to reject heat. Meanwhile, no one has yet produced a guard that combines infrared transparency with economy and durability for construction. So, are they necessary? Our measurements in the cavity suggest that the convection guard produced some unhelpful overheating in the daytime. This overheating could be attributed in part to the presence of solar-absorptive elements other than the radiator inside the convection guard, like the desiccant bags, and might have been minimized by changing its design. The sub-ambient cooling performance may also have been improved by using a radiator with higher solar reflectance. For reference, our radiator had a solar reflectance of 93.8% (Materials and Methods), whereas radiative cooling paints report a solar reflectance of 98% (5). This could lead to enough cooling where the convection guard helps during the day. In which case, adding a second layer of infrared-transparent film may help further. Nonetheless, our results suggest that convection guards may be an unnecessary complication with diminishing returns for this kind of real roof application, at least on sites where wind exposure is mild.

It would therefore be interesting to replicate the study without a convection guard and more thermal mass in the roof, at the amount we predict will stabilize the interior temperature. One effect that might influence the sky-facing heat balance in this scenario is dewfall powered by radiative cooling and then evaporation powered by sunshine (41, 42). While late-night dewfall would add latent heat to the radiator, surface evaporation could help cool the radiator in the morning. Dewfall could also promote self-cleaning on a super-hydrophobic radiator, helping to maintain spectral efficiency over the building's lifetime (43, 44).

It is important to emphasize that this study is focused on hot, dry climates. Not only are skies colder and winters milder in these climates, but indoor humidity is less of a concern, not just for thermal comfort and heat stress, but for the risk of condensation forming on cool, interior surfaces, which, if moisture lingers, can lead to mold growth and serious respiratory health problems. Regular air changes are essential in this regard, and we have shown how to produce these naturally while balancing the interior temperature. Dehumidification may be necessary at times in the room, with the added benefit that it can be used to reduce the wet bulb temperature during dangerous heat stress events (45–47).

The idea of self-cooling, self-venting buildings, which are simple by design and straightforward to build, is attractive. But it is important to recognize that there are limits to radiative cooling and that natural ventilation is not always possible, or necessarily healthier than mechanical ventilation. Outdoor air dilutes contaminates with indoor sources but brings in outdoor contaminants that may be hazardous, such as ozone and particulate matter. There is no reason our model cannot be applied with forced ventilation, allowing the air to be filtered. But it is worth noting that virtually any air treatment method has both benefits and risks associated with it. Material collected on

mechanical filters can interact with chemicals in the air to create secondary contaminants, and even germicidal light photochemistry can produce by-products (48). The industry lacks a comprehensive view of all these measures, to help inform decisions about what should be used under what circumstances. But one thing that is set to change in the aftermath of the COVID-19 pandemic is the recommended rate of outdoor air changes, which are likely to increase for every kind of building (17).

Removing insulation from a roof structure made from concrete, steel, or vaulted tiles may seem like a crude and counterintuitive proposition at first. But it could be relevant in hot and dry climates for a broad range of civic, commercial, and domestic spaces, such as market halls, community centers, low-rise condos with covered courtyards, attic spaces that pre-cool fresh air, or cold rooms that provide respite from heat waves. More generally, our work points to the need to re-examine basic assumptions on building insulation when accounting for new material capabilities that alter the flows of radiant heat between the building and its environment. There are no universal solutions to sustainable cooling, so we must also challenge universal ideas of thermal comfort (49). The infrastructure needed to produce constant and narrow temperature ranges, in every room, all the time, is not a pattern that can be thoughtlessly replicated. If the climate is very hot, hybrid approaches are also possible, where some rooms are climate controlled (and therefore need full insulation), while adjacent spaces make use of passive cooling measures, old or new (50). In these buildings, where spaces follow a thermal hierarchy (51), the aim of passive cooling may not be comfort per se, but guaranteeing better or safer conditions than outdoors as part of a diverse range of indoor thermal environments (52, 53). This can work knowing that in very hot weather, occupants can adapt by changing what they are doing or moving to a different room (34). The design of built infrastructure determines whether cooling technologies can operate efficiently. But skillful passive design can also influence behavior more broadly, helping to reduce temperature demand, nudge thermal expectations, leverage cultural adaptations to heat, and save lives when extreme heat coincides with blackouts (3, 33, 49).

Materials and Methods

Installation and box design

The test boxes were installed on a T-Slotted aluminum frame, which lifted them 0.34 m above the roof of the shipping container in Topanga Valley, California (34.118063, -118.579955). The container was covered with a light-colored tarpaulin to limit heat radiation to the bottom of the boxes. White PVDF-coated aluminum sheets were mounted on the T-Slotted aluminum frame as cladding to protect the boxes from sun exposure. The cladding was partially perforated, and did not touch the boxes, to create a ventilated cavity, so the outer surface of the boxes would not exceed ambient temperature. Sensors were mounted on the frame next to the boxes to measure wind (Atmos 22 anemometer), air temperature and relative humidity (Apogee EE08-SS with an aspirated radiation shield), ambient pressure (Apogee SB-100), and incoming long and shortwave radiation (Apogee SL-510-SS and SP-510-SS).

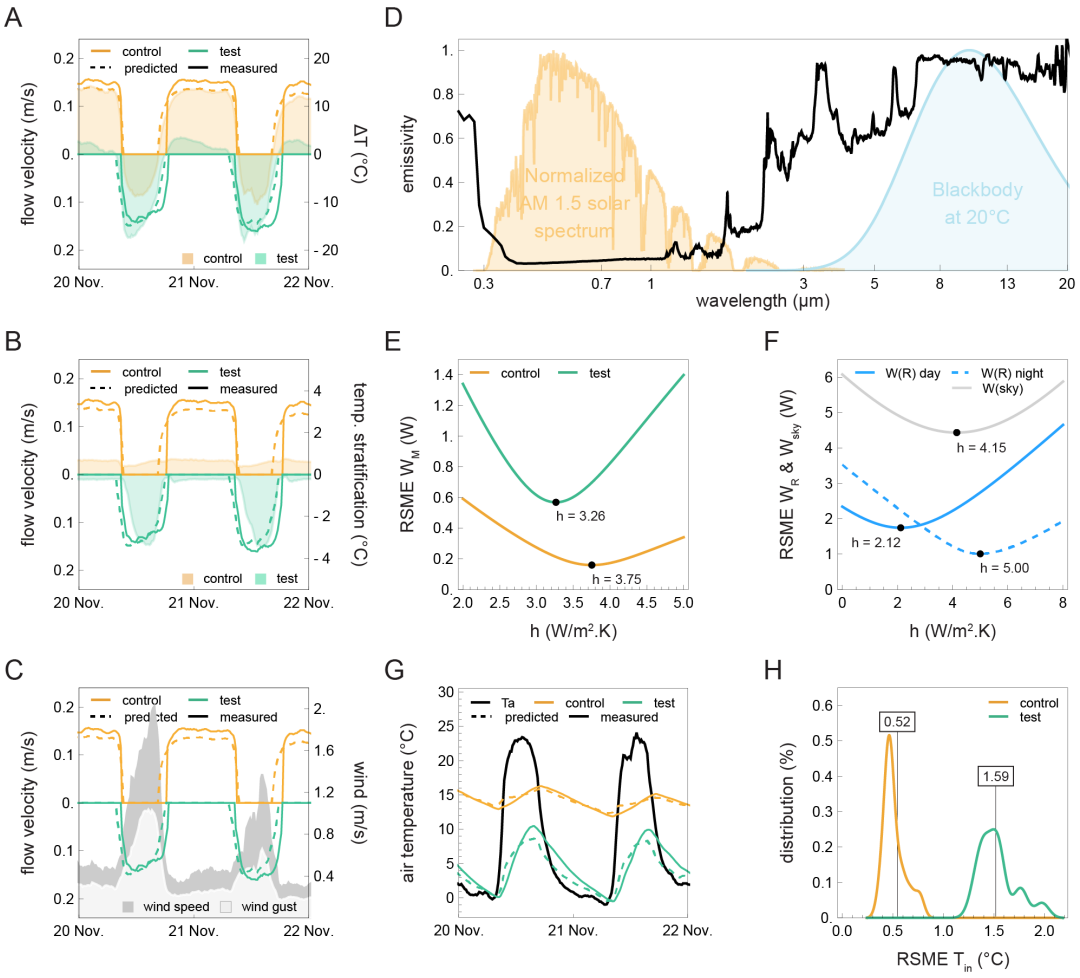

Figure 5. Performance characteristics and model calibration. **(A)** Comparison of the flow velocity measured in the inflow pipe-vents with the temperature difference between the ambient and the interior temperature ΔT. The ventilation stacks in the control (yellow) were designed to ventilate only when ΔT >0. Inversely, the test box (green) was designed to ventilate only when ΔT <0. **(B)** Comparison of the flow velocity with the temperature stratification measured at 0.1 and 0.2 m inside the boxes. The ventilation stacks were designed to produce well-mixed indoor thermal conditions. The stratification in the test boxes was likely due to the radiator overheating during the day. **(C)** Comparison of the flow velocity with wind gust (m/s) and speed (m/s). Both sets of stacks were designed to be wind-insensitive. **(D)** Wavelength-dependent emissivity of the radiative cooling material measured at near-normal incidence. **(E)** Calibration of the heat transfer coefficient on the internal thermal mass to minimize the error (*RSME*) between W_M measured and predicted from Eq. 5. *RSME* is defined in Eq. 13. **(F)** Calibration of the heat transfer coefficient on the soffit and top surface of the radiator to minimize the error between W_R and W_{sky} measured and predicted from Eq. 7 and 9, respectively. **(G)** Comparison of the measured and predicted T_{in} in the control and test boxes for two typical days in November 2022. **(H)** Distribution of the daily *RSME* for T_{in} in the control and test boxes for the 14-day experiment in November 2022. In the test box, the predictions underestimated the measurements by 1.58 °C on average, compared to 0.52 °C in the control box.

The interior space inside each box consisted of an air-tight 0.3 x 0.6 x 0.3 m enclosure, made of 2 mm thick thermoplastic polyester (PETG). The inside of the enclosure was lined with aluminum foil tape to limit radiative heat exchanges. The outside was covered with two layers of 24 mm vacuum-insulated panels (Panasonic U-Vacua™ Series VIPs) with a total U-value of 0.04 W/m^2.K to minimize heat transfer through the envelope (W_E). The enclosure was installed inside a 0.53 x 0.76 x 0.45 m waterproof case (Pelican iM3075 Storm Transport Case). The space between the case and the VIPs panel was filled with ~30 mm thick polyurethane ether foam. A heat flux and surface

temperature sensor (Huskeflux FHF04) was mounted at mid-height on one of the interior walls and two thermistors (Apogee ST-100) measured air temperature at 0.1 and 0.2 m inside the enclosure. The internal heat source in each box was a self-calibrating heat flux sensor with an integrated 1.2 W heater (Huskeflux FHF04SC). The thermal mass in each box was 4 x 1-liter water bottles (Smartwater) wrapped in aluminum foil tape for the September experiment, and we added 2 additional bottles in each box before the November experiment. The total surface area of the water bottles in thermal contact with the interior air was 0.26 and 0.40 m^2 for the September and November experiment, respectively. A heat flux and surface temperature sensor (Huskeflux FHF04) was mounted at mid-height on one of the bottles in each box.

Ventilation design

The ventilation stacks were two PVC pipes with 39 mm interior diameter, 0.2 and 0.13 m long, respectively. The short stack was the outflow vent and was mounted flush with the PETG enclosure. The long stack was the inflow vent and protruded 0.66 mm inside the PETG enclosure. The buoyancy column driving the ventilation was 0.13 m and corresponds to the height difference between the bottom of the inflow vent and the top of the outflow vent. Chimney caps protected both sets of stacks from rain and radiation from the surroundings. Sensors were measuring air temperature and wind velocity midway in each of the four stacks at the center of their cross-section. We derived the flow rate (Q) from the flow velocity (u) as $Q = A^* u$, with $A^* = cd\ A$ where A is the cross-section area of the pipe-vent, and c_d is as discharge coefficient accounting for the loss in pressure across the ventilation loop. We estimated the latter with $c_d = \sqrt{\sum_i \zeta_i}$ where ζ_i are coefficients for the friction resistance and local pressure losses at the entrance and exit of each vent-pipes (54). The discharge coefficients c_d are 0.49, and 0.47 for the control and test boxes, respectively. The associated A^* were used with Eq. 2 and 3 to predict the flow rate (Q) and ventilation heat transfer (W_V) from the temperature difference between the interior and exterior in the calibrated model. In Figure 5 A to C, those predictions are shown to be in good agreement with the measurements.

We designed our pipe-vents to have similar effects on the interior as buoyancy-driven mixing ventilation, but with unidirectional flow in the ventilation stacks. Typically, mixing ventilation entails using a single opening as both inlet and outlet, causing the air entering the room to instantaneously mix with the outgoing air (28, 29). This approach produces uniform indoor air temperature and is inherently sign-dependent, but it also complicates the measurement of flow rate because of turbulence in the vents and creates significant pressure losses. With two ventilation stacks, the test box still produced sign-dependent ventilation because the interior air could only escape through the pipe-vents at the bottom of the box when it was denser (or cooler) than the ambient air. During the day, negative buoyancy pressure drove warm air out of the short stack while sucking cold ambient air through the long stack. The same occurred in the control but for the opposite temperature sign since the pipe-vents were at the top of the box (Figure 5 A).

For the ventilation to produce uniform indoor air temperature, we adjusted the length of the long pipe-vent protruding inside the test box so it would end below the level at which the indoor air would naturally stratify. As such, we expected the plume of incoming warm exterior air to entrain some of the cold air from the stratified layer up and therefore help to maintain well-mixed thermal conditions inside (30). As shown in Figure 5B, this strategy was more successful in the control box, where the temperature difference between the top and bottom of the enclosure remained under 1 °C. In the test box, the temperature stratification reached up to 3 °C when the ventilation was flowing, but we believe this might have been amplified by overheating of the radiator soffit in the afternoon. Lastly, for the ventilation to remain primarily driven by thermal buoyancy and less sensitive to wind, we installed the two pipe-vents close to one another, with their exterior end almost flush with the waterproof case. Since the wind pressure difference between the two openings was minimal, the ventilation flow was unaffected by wind speed changes or gusts during the experiment (Figure 5C).

Radiator design

The sky radiator was a low-cost multilayered daytime radiative cooling material spray glued on a 6 mm thick 0.46 x 0.69 m aluminum plate. The material was a porous polyethene-based white material, with a thermally emissive fluoropolymer film bonded to it. The wavelength-dependent absorptivity/emissivity of the radiator is shown in Figure 5D. The spectral properties were measured with Perkin Elmar Lambda 950 UV-Vis-NIR spectrophotometer with an integrating sphere module for the 0.2-1.5 μm range. A Bruker Invenio R FT-IR spectrophotometer with an integrating sphere and MCT detector from IR associates was used for the rest of the wavelengths up to 20 μm. We assumed $\epsilon = 0.90$ for the rest of the spectrum, since fluoropolymers are emissive in that range. All the measurements were done with light at near-normal incidence, or almost perpendicular to the surface. The actual solar reflectance and thermal emittance of the radiator could therefore be slightly higher in the shortwave range and slightly higher in the longwave range if all angles of incidence were accounted for. To model the heat fluxes at the top surface of the radiator, we calculated the solar absorptivity $\alpha = 0.062$ (0.3-2.5 μm) based on the AM 1.5 Global solar spectrum, and the emissivity $\epsilon = 0.916$ (5-20 μm) based on the spectral intensity emitted by a blackbody at 20 °C (Figure 5D).

The radiator plate was mounted inside an acrylic module and rested on top of the PETG enclosure. An infrared transparent polyethylene (PE) film (~20 μm thick, with an estimated average transmissivity of ~85% (40)) was stretched 35 mm above the radiator plate. Forty-two 28g Silica gel desiccant bags were placed inside the acrylic module (under the PE film and around the radiator) to avoid condensation. The underside of the radiator was directly exposed to the interior, with a surface area of 0.2 m^2. This soffit was covered with aluminum foil tape like the rest of the PETG enclosure to limit radiative heat exchange between internal surfaces. A heat flux and surface temperature sensor was mounted at the center point on both sides of the radiator aluminum plate (under the radiative cooling material and under the aluminum foil tape).

Author Contributions: S.C. and R.F. designed the research. R.F. performed the research. J.M. and A.P.R. manufactured the radiative cooling material and measured the spectral properties. R.F. and S.C. analyzed the research data. R.F and S.C. wrote the original draft of the paper. J.M. and A.P.R. reviewed and edited the paper.

Acknowledgments: We would like to thank John May and Zeina Koreitem for hosting the experiment, Michael Scarborough for help with onsite maintenance, and Victoria Desgagné for help with designing and assembling the test boxes. S.C acknowledges support from the Canada Foundation for Innovation (2020 CFI Innovation Fund), McGill Sustainability Systems Initiative (MSSI), and the Natural Sciences and Engineering Research Council of Canada (NSERC Discovery Grant) under Grant No. RGPIN-2022-04490. A.P.R. acknowledges support from the National Science Foundation (NSF CAREER) under Grant No. 2146577, and the Sloan Research Fellowship (Alfred P. Sloan Foundation).

References

1. M. O. McLinden, C. J. Seeton, A. Pearson, New refrigerants and system configurations for vapor-compression refrigeration. *Science* **370**, 791–796 (2020).

2. L. W. Davis, P. J. Gertler, Contribution of air conditioning adoption to future energy use under global warming. *Proc. Natl. Acad. Sci.* **112**, 5962–5967 (2015).

3. IEA, "The Future of Cooling" (2018) (December 13, 2021).

4. T. Li, *et al.*, A radiative cooling structural material. *Science* **364**, 760–763 (2019).

5. J. Mandal, Y. Yang, N. Yu, A. P. Raman, Paints as a Scalable and Effective Radiative Cooling Technology for Buildings. *Joule* **4**, 1350–1356 (2020).

6. D. Han, *et al.*, Sub-ambient radiative cooling under tropical climate using highly reflective polymeric coating. *Sol. Energy Mater. Sol. Cells* **240**, 111723 (2022).

7. J. Mandal, *et al.*, Hierarchically porous polymer coatings for highly efficient passive daytime radiative cooling. *Science* **362**, 315–319 (2018).

8. A. P. Raman, M. A. Anoma, L. Zhu, E. Rephaeli, S. Fan, Passive radiative cooling below ambient air temperature under direct sunlight. *Nature* **515**, 540–544 (2014).

9. Y. Zhai, *et al.*, Scalable-manufactured randomized glass-polymer hybrid metamaterial for daytime radiative cooling. *Science* **355**, 1062–1066 (2017).

10. X. Huang, J. Mandal, A. Raman, Do-it-yourself radiative cooler as a radiative cooling standard and cooling component for device design. *J. Photonics Energy* **12**, 012112 (2021).

11. Y. Chen, *et al.*, Colored and paintable bilayer coatings with high solar-infrared reflectance for efficient cooling. *Sci. Adv.* **6**, eaaz5413 (2020).

12. D. Zhao, *et al.*, Subambient Cooling of Water: Toward Real-World Applications of Daytime Radiative Cooling. *Joule* **3**, 111–123 (2019).

13. E. A. Goldstein, A. P. Raman, S. Fan, Sub-ambient non-evaporative fluid cooling with the sky. *Nat. Energy* **2**, 1–7 (2017).

14. Y. Wu, *et al.*, A review of the application of radiative sky cooling in buildings: Challenges and optimization. *Energy Convers. Manag.* **265**, 115768 (2022).

15. H. Fang, *et al.*, Performance evaluation of a metamaterial-based new cool roof using improved Roof Thermal Transfer Value model. *Appl. Energy* **248**, 589–599 (2019).

16. A. R. Gentle, G. B. Smith, A Subambient Open Roof Surface under the Mid-Summer Sun. *Adv. Sci.* **2**, 1500119 (2015).

17. The Lancet COVID-19 Commission Task Force on Safe Work, Safe School, and Safe Travel, "Proposed Non-infectious Air Delivery Rates (NADR) for Reducing Exposure to Airborne Respiratory Infectious Diseases" (2022).

18. D. Zhao, *et al.*, Radiative sky cooling: Fundamental principles, materials, and applications. *Appl. Phys. Rev.* **6**, 021306 (2019).

19. F. Trombe, Devices for lowering the temperature of a body by heat radiation therefrom (1967) (March 15, 2023).

20. S.-Y. Heo, *et al.*, A Janus emitter for passive heat release from enclosures. *Sci. Adv.* **6**, eabb1906 (2020).

21. P. Bouet, "Domestiquer l'énergie solaire Architecture, décolonisation et écologisme dans la France d'après-guerre, 1945-1986," Université Gustave Eiffel, Paris, France. (2022).

22. P. Bouet, A Silent Graph. Tracing the Algerian Past of French Solar Experiments. *ABE J. Archit. Eur.* (2021) https:/doi.org/10.4000/abe.8913 (March 15, 2023).

23. P. M. Cuce, S. Riffat, A state of the art review of evaporative cooling systems for building applications. *Renew. Sustain. Energy Rev.* **54**, 1240–1249 (2016).

24. J. M. Holford, A. W. Woods, On the thermal buffering of naturally ventilated buildings through internal thermal mass. *J. Fluid Mech.* **580**, 3–29 (2007).

25. B. Lishman, A. W. Woods, The effect of gradual changes in wind speed or heat load on natural ventilation in a thermally massive building. *Build. Environ.* **44**, 762–772 (2009).

26. S. Craig, The optimal tuning, within carbon limits, of thermal mass in naturally ventilated buildings. *Build. Environ.* **165**, 106373 (2019).

27. T. de Toldi, S. Craig, L. Sushama, Internal thermal mass for passive cooling and ventilation: adaptive comfort limits, ideal quantities, embodied carbon. *Build. Cities* **3**, 42–67 (2022).

28. T. Chenvidyakarn, *Buoyancy effects on natural ventilation* (Cambridge University Press, 2013).

29. P. F. Linden, G. F. Lane-Serff, D. A. Smeed, Emptying filling boxes: the fluid mechanics of natural ventilation. *J. Fluid Mech.* **212**, 309–335 (1990).

30. S. D. Fitzgerald, A. W. Woods, The influence of stacks on flow patterns and stratification associated with natural ventilation. *Build. Environ.* **43**, 1719–1733 (2008).

31. C. Gladstone, A. W. Woods, On buoyancy-driven natural ventilation of a room with a heated floor. *J. Fluid Mech.* **441**, 293–314 (2001).

32. ASHRAE, *ANSI/ASHRAE Standard 55-2017: Thermal Environmental Conditions for Human Occupancy* (ASHRAE, 2017).

33. T. Parkinson, R. de Dear, G. Brager, Nudging the adaptive thermal comfort model. *Energy Build.* **206**, 109559 (2020).

34. M. Vellei, R. de Dear, C. Inard, O. Jay, Dynamic thermal perception: A review and agenda for future experimental research. *Build. Environ.* **205**, 108269 (2021).

35. M. F. Ashby, *Materials and the environment: eco-informed material choice*, 2nd ed (Elsevier/Butterworth-Heinemann, 2013).

36. T. Chenvidyakarn, A. Woods, Top-down precooled natural ventilation. *Build. Serv. Eng. Res. Technol.* **26**, 181–193 (2005).

37. S. R. Livermore, A. W. Woods, On the effect of distributed cooling in natural ventilation. *J. Fluid Mech.* **600**, 1–17 (2008).

38. A. Bejan, *Convection heat transfer*, Fourth edition (Wiley, 2013).

39. D. A. Parker, H. C. Burridge, J. L. Partridge, J. N. Hacker, P. F. Linden, Vertically distributed wall sources of buoyancy. Part 2. Unventilated and ventilated confined spaces. *J. Fluid Mech.* **907** (2021).

40. J. Zhang, *et al.*, Cover shields for sub-ambient radiative cooling: A literature review. *Renew. Sustain. Energy Rev.* **143**, 110959 (2021).

41. M. Zhou, *et al.*, Vapor condensation with daytime radiative cooling. *Proc. Natl. Acad. Sci.* **118**, e2019292118 (2021).

42. J. Li, *et al.*, A tandem radiative/evaporative cooler for weather-insensitive and high-performance daytime passive cooling. *Sci. Adv.* **8**, eabq0411 (2022).

43. F. Geyer, *et al.*, When and how self-cleaning of superhydrophobic surfaces works. *Sci. Adv.* **6**, eaaw9727 (2020).

44. J. Song, *et al.*, Durable radiative cooling against environmental aging. *Nat. Commun.* **13**, 4805 (2022).

45. E.-S. Im, J. S. Pal, E. A. B. Eltahir, Deadly heat waves projected in the densely populated agricultural regions of South Asia. *Sci. Adv.* **3**, e1603322 (2017).

46. C. Mora, *et al.*, Global risk of deadly heat. *Nat. Clim. Change* **7**, 501–506 (2017).

47. M. Sadeghi, R. de Dear, G. Morgan, M. Santamouris, B. Jalaludin, Development of a heat stress exposure metric – Impact of intensity and duration of exposure to heat on physiological thermal regulation. *Build. Environ.* **200**, 107947 (2021).

48. L. Morawska, *et al.*, A paradigm shift to combat indoor respiratory infection. *Science* **372**, 689–691 (2021).

49. R. Khosla, *et al.*, Cooling for sustainable development. *Nat. Sustain.* **4**, 201–208 (2021).

50. E. Teitelbaum, *et al.*, Membrane-assisted radiant cooling for expanding thermal comfort zones globally without air conditioning. *Proc. Natl. Acad. Sci.* **117**, 202001678 (2020).

51. F. Suerich-Gulick, A. Halepaska, S. Craig, Cascading temperature demand: The limits of thermal nesting in naturally ventilated buildings. *Build. Environ.*, 108607 (2021).

52. E. Teitelbaum, P. Jayathissa, C. Miller, F. Meggers, Design with Comfort: Expanding the psychrometric chart with radiation and convection dimensions. *Energy Build.* **209**, 109591 (2020).

53. E. Teitelbaum, *et al.*, Addressing a systematic error correcting for free and mixed convection when measuring mean radiant temperature with globe thermometers. *Sci. Rep.* **12**, 6473 (2022).

54. I. E. Idel'chik, A. S. Ginevskiĭ, *Handbook of hydraulic resistance*, 4th ed. rev. and augmented (Begell House, 2007).